

Directional self-assembly of organic vertically superposed nanowires

Received: 16 May 2024

Accepted: 29 August 2024

Published online: 04 September 2024

 Check for updatesYing-Xin Ma¹ & Xue-Dong Wang¹ ✉

Organic crystal-based superimposed heterostructures with inherent multi-channel characteristics demonstrate superior potential for manipulating excitons/photons at the micro/nanoscale for integrated optoelectronics. However, the precise construction of organic superimposed heterostructures with fixed superimposed sites remains challenging because of the random molecular nucleation process. Here, organic vertically superimposed heterostructures (OSHS) with fixed superimposed positions are constructed via semi-wrapped core/shell heterostructures with partially exposed cores, which provide preferential nucleation sites for further molecular epitaxial growth processes. Furthermore, the relative length ratio from 21.7% to 95.3% between interlayers is accurately adjusted by regulating the exposed area of the semi-wrapped core/shell heterostructures. Significantly, these OSHS with anisotropic optical characteristics demonstrate well regulation of excitation position-dependent waveguide behaviors and can function as photonic barcodes for information encryption. This strategy provides a facile approach for controlling the nucleation sites for the controllable preparation of organic heterostructures and advanced applications for integrated optoelectronics.

The controllable fabrication of organic micro/nanostructures with precise spatial organization has attracted increasing research interest in material chemistry due to its potential value in advanced organic optoelectronics^{1–4}. Organic low-dimensional crystal-based heterostructures with specific geometric characteristics, such as multiblock^{5–7}, core/shell (C/S)^{8–10}, branch-type^{11–13}, and network structures¹⁴, have made disparate contributions to crystal surface interaction-guided integrated nanophotonics. As exemplified by previous studies, organic multiblock heterojunctions with color-graded spatial engineering can manipulate photons and electrons in a coaxial structure¹⁵. For instance, researchers have demonstrated a charge transfer doping layer at heterogeneous interfaces in organic coaxial heterostructures. This charge-transfer process involves the formation of a pair of charge carriers, which are expected to promote electron conduction and enhance the electrical conductivity of the coaxial nanocables¹⁶. Impressively, organic coaxial C/S heterostructures with further expanded heterojunction areas not only enable integrated modulation and processing of photonic signals but also enhance the stability/tunability of carrier collection⁹.

Nonaxial organic branches and network categories in low-dimensional heterostructures can better meet the multiport input/output requirements of optical signal processing and wavelength division multiplexing systems¹⁷. Hence, exploring how to construct organic heterostructures with desirable structural characteristics at the micro/nanoscale is a precondition for customizing the optimal charge/photon transport behavior for integrated optoelectronics.

To date, multitudinous research efforts have been made to develop controllable fabrication strategies, such as the one-pot hierarchical self-assembly strategy involving the regulation of noncovalent interactions^{18,19}, stepwise seeded epitaxial growth strategy²⁰, physical vapor transport (PVT)^{21,22}, inkjet printing^{23,24}, and photochromic strategy²⁵, to realize the preparation of organic low-dimensional heterostructures. Nevertheless, these strategies have a common shortcoming that needs to be solved urgently, i.e., only the growth sequence of heterojunctions is finely developed, but the precise modification of structural characteristics for organic low-dimensional heterostructures remains challenging. A representative example is the organic multilayer

¹Institute of Functional Nano & Soft Materials (FUNSOM), Jiangsu Key Laboratory for Carbon-Based Functional Materials & Devices, Soochow University, Suzhou, China. ✉ e-mail: wangxuedong@suda.edu.cn

micro/nanostructures with large and sharp heterogeneous interfaces, which indicate a distinct preponderance in confining and manipulating photons/electrons within parallel connections and interconnections. However, in terms of controllable preparation, on the one hand, the uncertainty of the superimposed positions (Fig. 1a) greatly limits the manipulation of photons/electrons^{26,27}. On the other hand, superposition only in the horizontal direction greatly limits the utilization of vertical space, which is not conducive to the development of spatial integration and three-dimensional optoelectronic information processing and communications. Impressively, researchers have realized the precise modification of organic branched microstructures with controllable branch sites by introducing a dislocation point as an oriented nucleation site into microstructures to preferentially deposit solute molecules along the dislocation line²⁸. Inspired by this success, the

precise fabrication of organic multilayer heterostructures with fixed relative positions between various layers by taking advantage of specific structure-induced molecular-oriented self-assembly is feasible.

Here, we propose a facile strategy for the oriented self-assembly of organic vertically superimposed heterostructures with fixed positions by using the semi-wrapped C/S heterostructures consisting of 1,2,4,5-tetracyanobenzene-4H-dithieno[3,2-b:2',3'-d]pyrrole (TDP) and 1,2,4,5-tetracyanobenzene-benzo[*c*]phenanthrene (THT) microrods. Due to the structural compatibility between TDP and THT cocrystals, the as-fabricated TDP microrods are added as seeded cores into a THT cocrystal-unsaturated solution as a shell-layer solution, resulting in semi-wrapped C/S heterostructures whose shell layer does not completely wrap the core layer. The partially exposed core within the semi-wrapped C/S heterostructures as initial building blocks provides

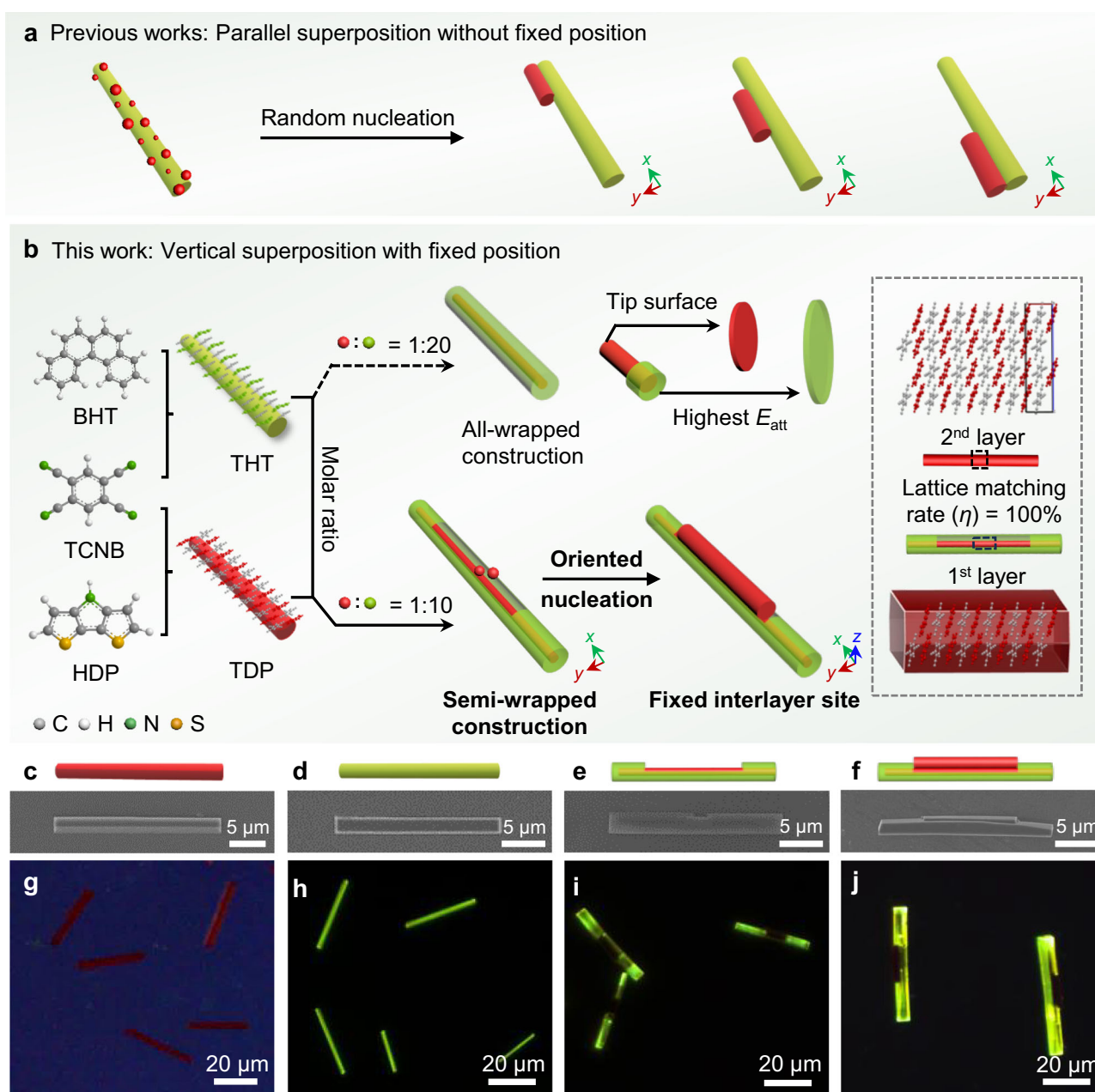


Fig. 1 | Illustration of the oriented epitaxial-growth of OSHs. a Schematic illustration: previous research on the fabrication of OSHs without a fixed interlayer position. **b** Schematic representation of the oriented nucleation strategy proposed in this work to construct OSHs with fixed interlayer positions. **c–f** SEM images of

c TDP microrods, **d** THT microrods, **e** TDP-THT semi-wrapped C/S microstructures, and **f** TDP-THT OSHs with fixed interlayer positions. **g–j** FM images of **(g)** TDP microrods, **(h)** THT microrods, **(i)** TDP-THT semi-wrapped C/S microstructures, and **(j)** TDP-THT OSHs with fixed interlayer positions.

preferential nucleation sites for the 2nd layer, and the 100% lattice matching ratio between the exposed core and 2nd layer triggers the corresponding epitaxial growth of organic superimposed heterostructures with fixed-layer sites (Fig. 1b). In development, the length ratio of the 2nd layer could be accurately regulated by increasing or decreasing the exposed area of the core section within semi-wrapped C/S heterostructures. Significantly, these as-fabricated OSHs possess waveguide behaviors related to the excitation position and are applied as photonic barcodes for photonic encryption. Therefore, the oriented nucleation triggered by high-energy metastable structures enables the accurate fabrication of organic superimposed heterostructures with fixed layer sites, which opens a universal avenue for exploring highly ordered organic micro/nanostructures.

Results

Strategies for the directional self-assembly of OSHs

The organic opto-functional molecules 4H-dithieno[3,2-b:2',3'-d]pyrrole (HDP) and benzo[c]phenanthrene (BHT) display strong electron-donating abilities (Supplementary Fig. 1). With the combination of electron-deficient 1,2,4,5-tetracyanobenzene (TCNB) molecules through charge-transfer (CT) interactions, HDP self-assembled into 1D red-emitting TDP microrods with a photoluminescence (PL) peak at 750 nm (Figs. 1c, g, and Supplementary Fig. 2). The calculated molecular orbitals (MOs) of the TDP cocystal are completely different from those of the independent TCNB and HDP molecules. Specifically, the energy diagram shows that the highest occupied molecular orbital (HOMO) (−5.60 eV) of the TDP cocystal is lower than that of the isolated HDP molecule (−5.15 eV), while the corresponding lowest unoccupied molecular orbital (LUMO) (−3.70 eV) is greater than that of the isolated TCNB molecule (−3.92 eV). This could be ascribed to the transfer of π -CT from the HOMO of HDP to the LUMO of TCNB, causing the charge to interact in the ground state, rearranging electrons to form entirely new MOs (Supplementary Fig. 3)²⁹. Additionally, the simulated crystallographic data revealed that the TDP crystal has cell parameters of $a = 7.3528 \text{ \AA}$, $b = 7.1026 \text{ \AA}$, $c = 29.5733 \text{ \AA}$, $\alpha = 90^\circ$, $\beta = 90.347^\circ$, and $\gamma = 90^\circ$ (Supplementary Table 1), and belongs to the P2₁/c space group and monoclinic system.

The BHT and TCNB molecules self-assembled into 1D green-emitting THT microrods (Figs. 1d, h, and Supplementary Fig. 2), and the PL peak was located at 560 nm. The lower HOMO energy (−5.86 eV) of the THT cocystal than that of the BHT molecule (−5.54 eV) and the higher LUMO energy (−3.62 eV) compared to that of the TCNB molecule (−3.92 eV) indicate the formation of entirely new MOs (Supplementary Fig. 4). The THT cocystal possesses cell parameters of $a = 7.2363 \text{ \AA}$, $b = 8.0530 \text{ \AA}$, $c = 16.9259 \text{ \AA}$, $\alpha = 88.451^\circ$, $\beta = 89.127^\circ$, and $\gamma = 87.740^\circ$ and belongs to the P $\bar{1}$ space group and triclinic system (Supplementary Table 2). The spatial PL spectra were adopted to calculate the CIE coordinates, which verified the fidelity of the emission colors in the fluorescence microscopy (FM) image (Supplementary Fig. 1), and the true emission colors of the TDP (0.72, 0.28) and THT (0.47, 0.51) microrods were obtained (Supplementary Fig. 5). These two TCNB-based cocystals both present one-dimensional (1D) structural features with intense body emission. These as-fabricated TDP and THT cocystals demonstrate PL lifetimes (τ) of 25.65 ns and 94.81 ns (Supplementary Fig. 6), respectively. Moreover, the photoluminescence quantum yields of 28.6% and 44.1% indicate superior optical performance.

Transmission electron microscopy (TEM) investigation revealed that the TDP and THT microrods (Supplementary Figs. 7a, 8a) both present a typical 1D structure with straight and long morphologies, which is consistent with the calculated morphology (Supplementary Figs. 9, 10). Furthermore, the apparent diffraction spots in the selected-area electron diffraction (SAED) diagrams (Supplementary Figs. 7b, 8b) indicate that these two microcrystals are highly crystalline and grow in the same direction [100]. The intense diffraction

peaks shown in the X-ray diffraction (XRD) patterns further verify the highly crystalline nature of the TDP and THT cocystals (Supplementary Figs. 11). Furthermore, the polarization patterns of TDP and THT cocystals with anisotropic properties also demonstrate high crystallinity (Supplementary Figs. 12). Notably, TDP and THT cocystals possess similar molecular packing patterns (Supplementary Figs. 13, 14), indicating high structural compatibility³⁰. On the strength of their structural advantages, TDP and THT cocystals contribute to the hetero-nucleation and epitaxial growth to construct organic heterostructures.

Nevertheless, the CT interactions of the TDP (−16.23 kcal mol^{−1}) and THT (−18.43 kcal mol^{−1}) cocystals are approximately equal. Similar weak interactions are more conducive to driving homogeneous nucleation of individual cocystals (Supplementary Figs. 15, 16) than hierarchical self-assembled heterostructures with precise spatial organization. Consequently, instead of a one-pot reaction, a multistep seeded self-assembly strategy is adopted to reasonably design and construct OSHs with precise spatial organization (Supplementary Fig. 17). Specifically, through a typical solvent evaporation method^{31,32}, red-emissive TDP cocystals are prepared and put into the system as preformed seed microrods. Then, green-emissive THT cocystals are added for epitaxial growth on the preexisting TDP microrods. As a result, semi-wrapped or all-wrapped organic C/S heterostructures (Supplementary Fig. 18) are obtained by controlling the relative molar ratio of THT and TDP cocystals. In detail, when the molar ratio of red-emitting TDP cocystals to green-emitting THT cocystals is 1:20, all-wrapped C/S heterostructures are formed, and when the ratio is 1:10, a certain amount of THT cocystals only partially epitaxially grow on the TDP microrods, exposing the core part at the center of the microrods and forming the semi-wrapped C/S heterostructures (Figs. 1e, i, and Supplementary Fig. 19). In development, the aforementioned semi-wrapped C/S heterostructures are added as 1st layer building blocks to a TDP cocystal-saturated supernatant, leading to the oriented epitaxial growth of TDP on the unwrapped core surface and eventually obtaining superimposed heterostructures with fixed interlayer positions on the *c*-axis (Figs. 1d, j).

Construction of semi-wrapped C/S heterostructures

Through a stepwise seeded self-assembly approach³³, organic semi-wrapped C/S heterostructures are controllably fabricated after green-emissive THT cocystals undergo selective heterogeneous nucleation and epitaxial growth on the surface of preexisting red-emissive TDP microrods. As illustrated in Fig. 2a, a certain amount of green-emissive THT cocystals are only partially selectively wrapped on the pre-fabricated TDP microrods, causing the exposure of a portion of the core part. The presence of well-defined semi-wrapped C/S heterostructures is preliminarily confirmed by the FM image in Fig. 2b. The FM image of the representative organic semi-wrapped C/S heterostructure (Fig. 2c) indicates that under excitation in the UV band (330–380 nm), the middle segment output red emitting and both ends outcouple green emitting. Under the excitation of green-light (500–550 nm), the entire axis of the rod-like structure emits bright and clear red-emission (Fig. 2d). This excitation wavelength-dependent emission is ascribed to spectral overlap between the excitation source and the intrinsic excitation spectra of the THT cocystal, which confirms the C/S structure at both ends and the exposed core in the middle.

Moreover, an obvious heterojunction between the C/S block and unwrapped block is clearly observed in the bright-field image (Fig. 2e). Scanning electron microscopy (SEM) observation visually revealed the smooth surface of the C/S block and the growth gap caused by the incomplete package (Fig. 2f and Supplementary Fig. 20). The spatially resolved PL spectrum in situ collected at the end of the heterostructure (marked as 1 in Fig. 2c) by focusing a laser beam ($\lambda = 380 \text{ nm}$) contains both green emission from the THT cocystal and red emission from the TDP cocystal (Fig. 2g), verifying the C/S block within the

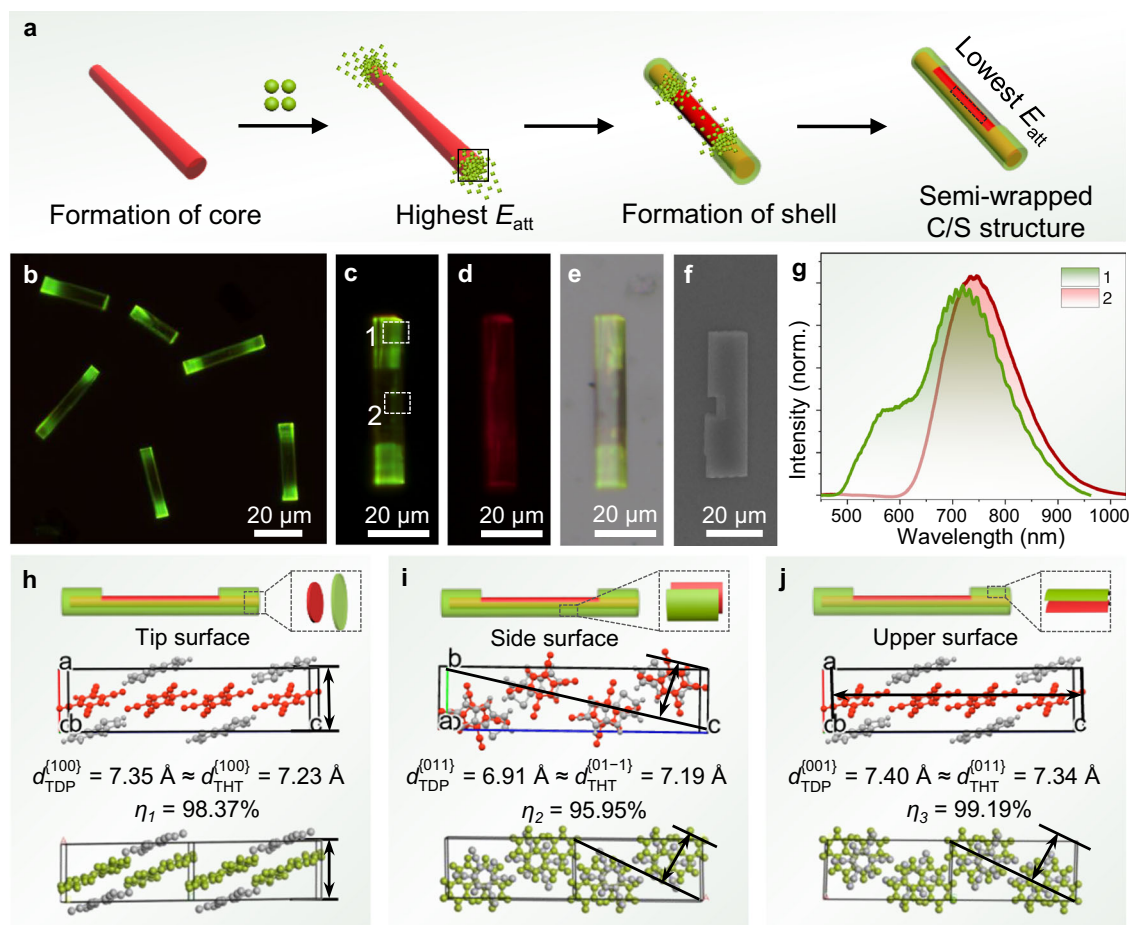


Fig. 2 | Structure and growth mechanism of semi-wrapped C/S heterostructure. **a** Illustration of the growth process of organic semi-wrapped C/S microrods. **b** FM image of TDP microrods partly wrapped by THT cocystals, scale bar: 20 μm . **c**, **d** FM images of an individual semi-wrapped C/S construction excited by (c) UV light (330–380 nm) and (d) green light (500–550 nm). Scale bars: 10 μm . **e** Bright-field micrograph of the corresponding semi-wrapped C/S heterostructure in

c, scale bar: 10 μm . **f** SEM micrograph of a typical semi-wrapped C/S heterostructure with an obvious unwrapped gap. **g** Corresponding PL spectra obtained from the tip and body sites labeled in (c). **h–j** Molecular packing arrangements and lattice matching rate (η) of TDP and THT cocystals at the (h) tip, (i) side, and (j) upper surface within the semi-wrapped C/S heterostructures.

heterostructure. However, the PL peak in the middle part of the microrod (marked as 2 in Fig. 2c) only shows red emission from the TDP cocystal, and the PL peak is located at 750 nm, convincingly demonstrating again that there is an unwrapped gap in the structure. Interestingly, the PL spectra at the tip position of the semi-wrapped C/S heterostructure exhibit a series of sharp fluorescence resonance peaks that indicate an optical cavity effect. This is because it contains a signal that resonates in the end part of the heterostructure. The cavity effect suggests the excellent light confinement property of the semi-wrapped C/S heterostructures, which is essential for the propagation of photon signals in optical circuits³⁴. These PL spectra are consistent with those of the individual TDP and THT cocystals depicted in Supplementary Fig. 2. The CIE coordinates obtained from the spectra of the C/S block (green line) and unwrapped core block (red line) are (0.52, 0.47) and (0.70, 0.27), respectively (Supplementary Fig. 21). Hence, organic semi-wrapped C/S heterostructures consisting of red-emissive TDP micro rods as the core and green-emissive THT cocystals as the shell are successfully fabricated by controlling the relative molar ratio of TDP and THT cocystals.

Notably, the mechanism of the facet-selective epitaxial growth process driven by lattice matching and surface-interface energy balance to construct semi-wrapped C/S structures is investigated in detail. As depicted in Fig. 2h, the (100) crystal surfaces of the TDP cocystal and THT cocystal adopt similar molecular packing modes,

contributing to the large lattice matching rate ($\eta_1 = 1 - |7.35 - 7.23| / 7.35$) of 98.37%, resulting in preferential epitaxial growth on the tip surfaces of the TDP microrod. Moreover, considering the surface-interface energy balance, THT molecules preferential hetero-nucleation at the (100) tip surface with the highest attachment energy in the TDP crystal ($|E_{\text{attach}}^{\text{TDP}}\{100\}_s = -65.37| \text{ kcal mol}^{-1} > |E_{\text{attach}}^{\text{TDP}}\{011\}_s = -54.22| \text{ kcal mol}^{-1} > |E_{\text{attach}}^{\text{TDP}}\{002\}_s = -24.60| \text{ kcal mol}^{-1}$) to eliminate unstable surfaces (Supplementary Table 3), achieving a thermodynamically favorable state³⁵. Furthermore, the side surface of the TPD crystal adopts a low lattice mismatching rate ($\eta_2 = |6.91 - 7.19| / 6.91 = 4.05\%$) with the side surface of the THT crystal (Fig. 2i), facilitating further epitaxial growth of the THT crystals. Moreover, the similar lattice constants ($\eta_3 = 1 - |7.40 - 7.34| / 7.40 = 99.19\%$) of the upper crystal planes in the two growth morphologies are also beneficial for the epitaxial growth process (Fig. 2j). Nevertheless, the (001) upper surface of the TDP crystal possesses the lowest surface attachment energy (Supplementary Table 3), causing exposure of the upper surface in the case of insufficient THT molecules, i.e., unwrapped core blocking in the heterostructures.

Directional self-assembly process of OSHs

Then, the self-assembled high-energy metastable organic semi-wrapped C/S heterostructures act as building blocks for the further oriented homogeneous nucleation of TDP cocystals. Specifically,

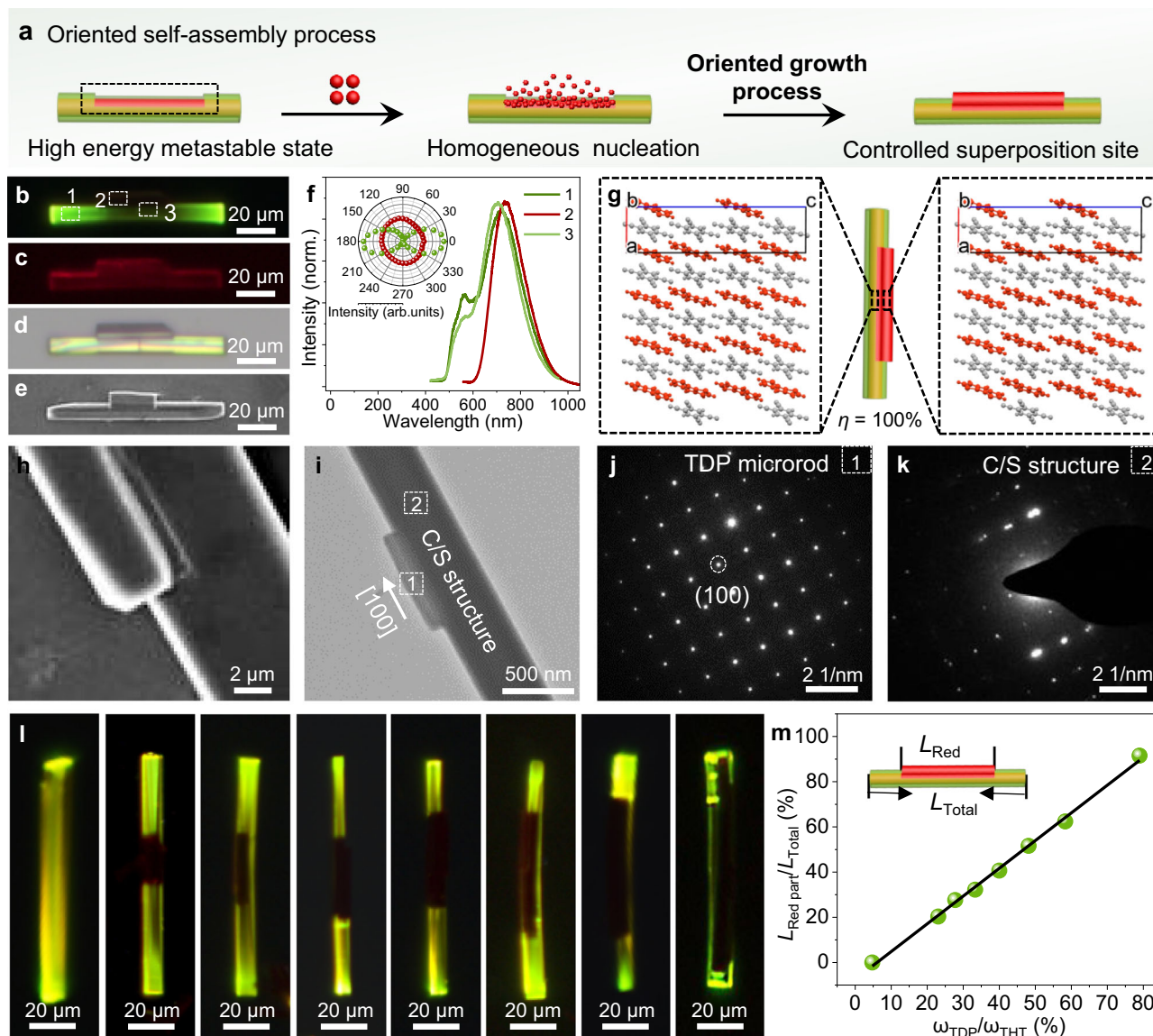


Fig. 3 | Growth mechanism analysis and quantitative regulation of the OSHs. **a** Illustration of the oriented integrated process of OSHs constructed on the basis of semi-wrapped C/S heterostructures. **b–d** FM images of a typical superimposed heterostructure under the excitation of **(b)** UV and **(c)** green light. Scale bars: 10 μm . **d** Bright-field micrograph of the corresponding OSH, scale bar: 10 μm . **e** SEM micrograph of a typical OSH. **f** Corresponding PL spectra gathered at different positions labeled in **b**. Inset: the corresponding polar image of the peak intensity. **g** Molecular packing arrangement and direction at the heterojunction area of the superimposed heterostructure. **h** SEM image of a typical heterojunction area within an OSH. **i** TEM micrograph of an individual OSH. **j, k** SAED patterns of the **(j)** 2nd layer and the **(k)** 1st layer within the superimposed structure. **l** FM images of organic superimposed heterostructures with increasing red region length from left to right. **m** Plot of the length ratio for the red part within the whole structure versus the molar ratios of TDP and THT cocrystals.

g Molecular packing arrangement and direction at the heterojunction area of the superimposed heterostructure. **h** SEM image of a typical heterojunction area within an OSH. **i** TEM micrograph of an individual OSH. **j, k** SAED patterns of the **(j)** 2nd layer and the **(k)** 1st layer within the superimposed structure. **l** FM images of organic superimposed heterostructures with increasing red region length from left to right. **m** Plot of the length ratio for the red part within the whole structure versus the molar ratios of TDP and THT cocrystals.

these as-prepared semi-wrapped C/S heterostructures offer a high-energy unwrapped gap that facilitates the oriented self-assembly of organic molecules. As a result, when additional TDP molecules are added to the system of these as-prepared semi-wrapped C/S heterostructures, the TDP molecules preferentially undergo homogeneous nucleation at the unwrapped gap, eventually realizing organic superimposed heterostructures with fixed interlayer positions on the *c*-axis (Fig. 3a). As shown in Fig. 3b, the long microrod of the 1st layer exhibits yellow–green emission, which is consistent with the aforementioned semi-wrapped C/S heterostructure, and the short microrod of the 2nd layer exhibits red emission, which is consistent with the TDP cocrystal upon excitation with UV light. However, under the excitation of green light, the entire superimposed heterostructure exhibited bright and clear red emission (Fig. 3c). It is preliminarily proven that the formation of a superimposed heterostructure is based on the presence of a semi-wrapped C/S structure, which is further formed by an oriented self-

assembly process in the unwrapped area. The bright-field and SEM images given in Figs. 3d, e intuitively display the heterojunction between the 1st layer and 2nd layer. Furthermore, the PL spectra of the long microrod (labeled as 1 in Fig. 3b) exhibit PL peaks at 560 and 735 nm, which is consistent with the PL spectra of the semi-wrapped C/S heterostructure (Fig. 3f). The short microrod (labeled as 2 in Fig. 3b) presents a PL peak at 750 nm, which is in accordance with the PL peak of an independent TDP crystal (Supplementary Fig. 2). Moreover, the PL spectra collected at the hetero-interface contain both green emission from THT and red emission from the TDP crystal, demonstrating that the superimposed heterostructures were successfully constructed.

Significantly, the contact surface with the same packing arrangement and orientation between the 1st and 2nd layers contributes to a 100% lattice matching rate (Fig. 3g), revealing the tendency for these two layers to exhibit an oriented combination. Notably, the interlayer position control is induced by unwrapped growth gaps within the

semi-wrapped C/S heterostructure, rather than the 100% lattice matching mentioned above. The semi-wrapped C/S heterostructures, as a kind of high-energy metastable structure, induce the preferential nucleation of molecules at the growth gap to eliminate unstable surfaces, achieving a thermodynamically favorable state. An ultralow lattice mismatch ratio below 5% is a prerequisite for the construction of heterogeneous structures. Therefore, the oriented growth process can be theoretically realized by selecting materials with lattice matching rates greater than 95% with the exposed core part.

As illustrated in Fig. 3h, as the 1st layer of the OSHs, the semi-wrapped C/S heterostructure has an obvious groove, providing a preferential nucleation site for the growth of the 2nd layer structure. The TEM image (Fig. 3i) clearly shows a distinct superimposed heterostructure with disparate layer lengths, and the corresponding SAED spots (Fig. 3j) of the short microrod (marked as 1) present a pattern identical to that of the TDP microrod growing along the same direction as [100]. In contrast, the diffraction spots of the long microrod (marked as 2) are disordered (Fig. 3k). The disordered diffraction spots are attributed to the lattice superposition of the core section and shell section, which changes the molecular-stacking orientation. Moreover, the XRD pattern (Supplementary Fig. 11) of the superimposed structures contains the characteristic peaks of both TDP and THT cocystals. These data successfully demonstrate the feasibility of utilizing semi-wrapped C/S heterostructures to induce the oriented self-assembly of OSHs with specific interlayer sites.

Notably, the length of the 2nd layer (red part) within the OSHs is quantitatively adjusted by modulating the molar ratio of TDP to THT during the self-assembly process of the 1st layer. Take an example, a 100 μL TDP mixed solution with a concentration of 2.0 mmol L^{-1} was dropped on a quartz substrate, and after the crystallization time was 60 s, a 1500 μL THT mixed solution at a concentration of 2.0 mmol L^{-1} was dropped onto a quartz substrate with crystallized TDP cocystal. When the crystallization time reached 60 s, 350 μL of the TDP mixed solution was dropped onto the substrate again, and when the solvent evaporated completely, organic vertically superposed heterostructures with a length ratio of 21.7% were observed. For another example, a 100 μL TDP mixed solution was dropped on a quartz substrate, and after the crystallization time was 60 s, 300 μL of the THT mixed solution was dropped onto a quartz substrate with a crystallized TDP cocystal. When the crystallization time reached 60 s, 650 μL of the TDP mixed solution was dropped onto the substrate again, and when the solvent evaporated completely, vertically organic superposed heterostructures with a length ratio of 95.3% were observed.

As shown in Fig. 3l, the length of the red-emitting 2nd layer is inversely proportional to the proportion of THT cocystals. In fact, during the construction of the 1st semi-wrapped C/S heterostructures, the exposed degree of the core segment is increased or decreased by decreasing or increasing the proportion of THT cocystals, respectively, thereby regulating the length of the 2nd layer in the superimposed heterostructures. As indicated in Fig. 3m, the length ratio of the 2nd layer linearly depends on the ratio between the TDP and the THT cocystal. Consequently, according to this linear relationship, the relative length ratio from 21.7% to 95.3% of the different layers in the superimposed structure can be reasonably controlled by accurate quantitative manipulation of the ratio of TDP to THT crystals.

Application of photonic barcodes in OSHs

The heterojunction interface of organic heterostructures is the key component for photon input and output in modern optoelectronics³⁶, as in the case of photonic switches^{37,38}, optical routers^{39,40}, and wavelength converters⁴¹. Significantly, the coupling of excitons and photons is an effective approach for regulating the optical transmittance of organic active waveguides at low power density^{42,43}. As shown in Fig. 4a, the greater energy gap of green-emissive THT cocystal than that of red-emissive TDP cocystal is conducive to the energy transfer

(ET) process from THT to TDP cocystals. Moreover, the close coincidence of the THT emission spectra and TDP absorption spectra (Supplementary Fig. 2) indicated that energy transfer could occur via either the short-range Dexter mechanism ($< 1 \text{ nm}$) or the long-range Förster resonance energy transfer (FRET) process. However, the short-range Dexter mechanism could not account for the current system, which shows a high energy transfer efficiency at an almost negligible TDP doping ratio, indicating long-range energy transfer. The energy transport by excitons in these as-prepared organic superposed heterostructures mainly involves a FRET process based on dipole–dipole coupling, which is ascribed to a long-range energy transfer process⁴⁴.

As shown in Supplementary Fig. 22, when combined with the TDP cocystal, the PL lifetime of the THT cocystal at 560 nm is significantly reduced from 94.81 to 70.07 ns. Comparatively, the PL lifetime at 750 nm of the TDP cocystals markedly improved from 25.65 to 34.15 ns after the formation of the heterojunction. The decrease in the PL lifetime of the THT cocystal occurs because of the increasing density of low-energy states for energy migration, i.e., the increase in TDP cocystals whose PL decay is faster when energy transfer occurs in heterostructures. The increase in the PL lifetime of TDP is attributed to the increased contribution of the THT cocystals, whose PL decay is substantially slower⁴⁵. The wavelength-dependent changes in the emission lifetime suggest effective energy transfer efficiency at 560 nm and 750 nm, indicating the involvement of exciton migration in the energy transfer process⁴⁶. Therefore, the excited excitons of the THT shell layer can be effectively transferred to the TDP core layer through an energy transfer process, resulting in orange emission (Fig. 4a).

Subsequently, the optical waveguide behaviors of TDP and THT cocystals were measured via homemade optical microscopy (Supplementary Fig. 23). In detail, bright green and red emissions are observed at the tips of the THT and TDP microrods, respectively, with a 380 nm laser beam locally excited along the axis of the organic microrods (Supplementary Fig. 24a, d). Accordingly, distance-dependent PL spectra are collected from the tips (Supplementary Fig. 24b, e), demonstrating that the PL intensity at the tip decreases gradually with increasing photon transmission distance. Furthermore, the optical-loss coefficients of single THT and TDP microrods ($R_{\text{THT}} = 0.174 \pm 0.003 \text{ dB}/\mu\text{m}$, $R_{\text{TDP}} = 0.130 \pm 0.004 \text{ dB}/\mu\text{m}$) are calculated using a single-exponential fitting $I_{\text{tip}}/I_{\text{body}} = A \exp(-Rd)$ ⁴⁷, where d represents the distance between the excitation point and emission tip. The low optical loss coefficients demonstrate the excellent photon confinement ability and good optical waveguide performance of these two TCNB-based cocystals.

Organic superimposed heterostructures composed of a TDP-THT semi-wrapped C/S heterostructure (1st layer) and a single TDP microrod (2nd layer) were prepared for the exploration of optical transmission behavior at the heterojunction. Accordingly, prototypical photonic barcodes based on an individual organic superimposed heterostructure have been proposed. As shown in Fig. 4a, four optical output channels are located on the two tips of the 1st layer and the 2nd layer. When excited at the center part of the 1st layer (Input I), the photon transmission to the 1st layer corresponds to the passive waveguide mode⁴⁸, leading to the spectra and polarizations at all channels being the same as those at the excitation positions (Figs. 4b, d). Moreover, the red luminescence at both tips of the 2nd layer structure displays an active optical waveguide mode with discrepant PL spectra and polarizations between the excitation position (Figs. 4b, d), indicating that the excitons of the THT are generated and that energy is transferred to the TDP during optical transmission via a FRET process. In contrast, when the 2nd layer (Input II) is excited, the passive waveguide mode causes the four channels in both the 1st and 2nd layers to produce spectra and polarization identical to those of the excitation positions (Figs. 4c, e). Hence, in the absence of the FRET process, red emission is observed in all channels of the 1st layer and 2nd layer in the

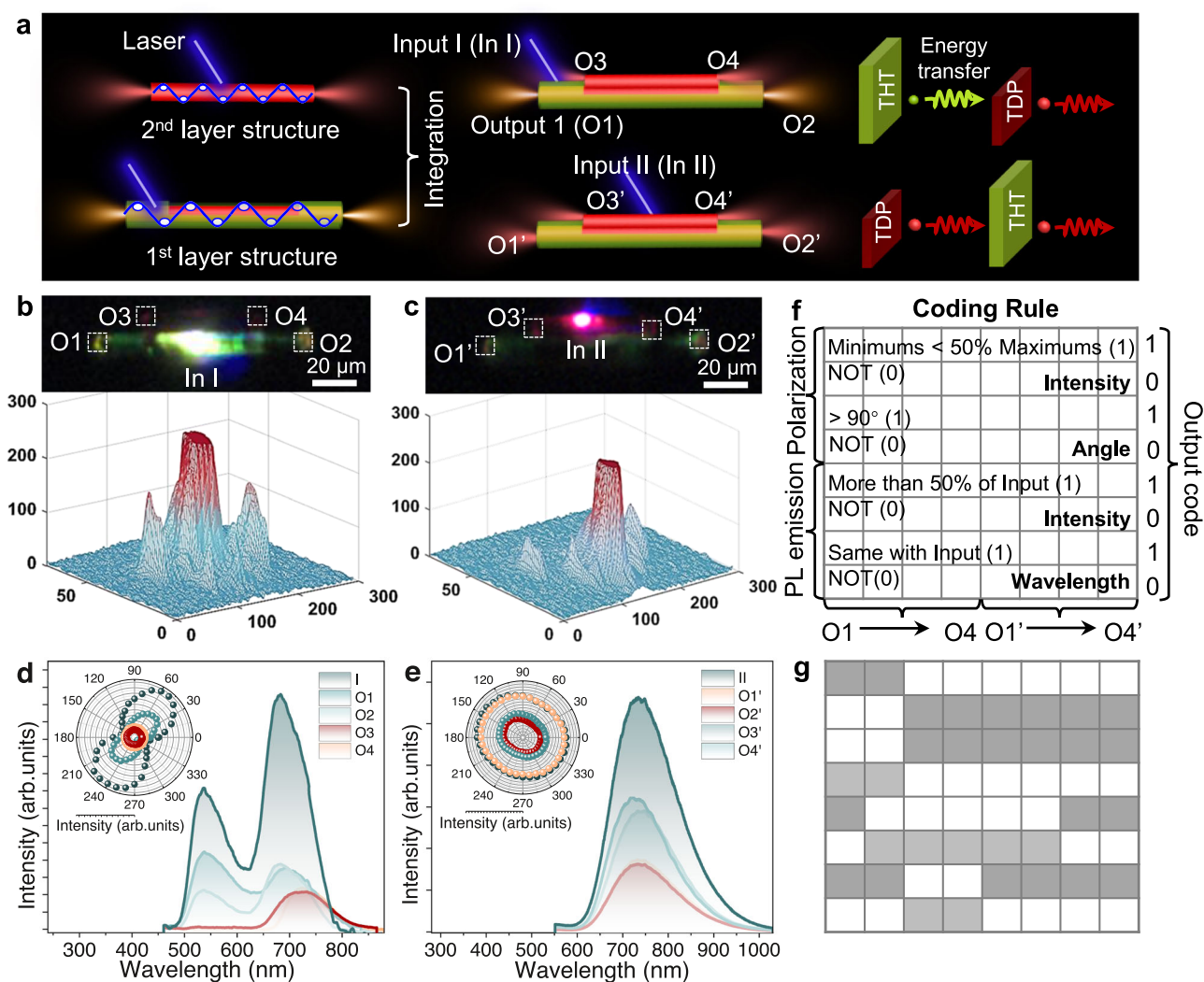


Fig. 4 | Optical barcode operation of OSHs. **a** Illustration of the optical transport behaviors within OSHs and the ET process from green-emissive THT to red-emissive TDP crystals. **b, c** FM images of the organic superimposed heterostructure excited by a focused laser at different sites and the corresponding PL intensity of the optical signal extracted by MATLAB software. **d, e** Spatially resolved PL spectra

of four output channels (O) corresponding to the **(d)** input I (In I) and **(e)** input II (In II) channels, as marked in **(b)** and **(c)**, respectively. Inset: the corresponding polar image of the peak intensities. **f** Illustration of the coding rule of the photonic barcode. **g** The barcodes of the organic superimposed heterostructure corresponding to **(d)** and **(e)**.

superimposed heterostructure. Notably, the photon efficiency is calculated based on the output couple spectrum and in situ spectrum⁴⁷. The efficiencies are calculated to be 93.8% and 89.2% when excited at In1 and In2, respectively. The high photon efficiency further reveals the low optical loss, which promotes the development of nanophotonic integrated optoelectronics.

For potential photonic applications, a multichannel information encoding function is achieved according to the obviously different emission and polarization signals. As shown in Fig. 4f, the output channels (O1-O4) on the left side of the horizontal coordinate correspond to input mode I, and the four output channels (O1'-O4') on the right side correspond to input mode II. Moreover, the vertical coordinate represents the wavelength and intensity of the PL emission and the angle and intensity of the polarization. Then, the excitation position-dependent waveguides that flexibly regulate the emission and polarization of the different output channels are collected as photonic barcodes. These optical parameters of the vertical axis represent two types of logical values, i.e., 0 and 1. In detail, the same PL spectral wavelength of both the output channel and excitation position is defined as 1, and conversely, it is defined as 0. Analogously, if the PL spectral intensity of the output signal is (or is not) greater than half of

the PL spectral intensity of the excitation position, the output signal is considered to be 1 (0). Furthermore, a polarization output signal $> 90^\circ$ relative to the rod direction is defined as 1, and conversely, is regarded as 0. For the polarization intensity, the output signal could be defined as 1 (0) when the lowest intensity is less (greater) than 50% of the highest intensity. These output values are filled based on the logical code of the signal from the output channels. Accordingly, photonic barcodes are achieved by summarizing the output signals of multiple output channels in the superimposed heterostructure (Fig. 4g). Consequently, optical interconnection heterostructures with anisotropic properties contribute to accurate regulation of optical signals within multiple input/output channels and promote the development of 2D photonic encryption devices.

Discussion

In summary, an oriented integrated process for organic superimposed heterostructures consisting of a semi-wrapped C/S heterostructure (1st layer) and a TDP microrod (2nd layer) was successfully achieved. The exposed core segment in the 1st layer provides preferential nucleation sites for the 2nd layer, and the lattice matching ratio between the two layers reaches 100%, which is conducive to the corresponding epitaxial

growth process. Furthermore, the relative length ratio between the 1st and 2nd layers is finely regulated by controlling the exposed area of the core part in the 1st layer. Significantly, these well-organized organic superimposed heterostructures realized the function of photonic barcodes for multichannel information processing on the basis of their anisotropic optical characteristics. The present work provides a strategy for controlling nucleation sites for the controllable fabrication of organic superimposed heterostructures, and offers potential applications by modulating optical transmission behaviors at heterogeneous interfaces, contributing to the development of integrated optoelectronics.

Methods

Controllably self-assembly of organic semi-wrapped core/shell heterostructures

0.02 mmol (3.6 mg) of TCNB and 0.02 mmol (7.2 mg) of HDP were dissolved into 10 mL of dichloromethane (DCM) at a concentration of 2.0 mmol L⁻¹ to obtain a TDP stock solution. Similarly, a THT stock solution was prepared by dissolving 0.02 mmol (3.6 mg) of TCNB and 0.02 mmol (4.6 mg) of BHT into 10 ml of DCM at a concentration of 2 mmol L⁻¹. Then, the TDP stock solution was added to 10 ml of ethanol (EtOH), and the mixture was dropped onto a quartz substrate with a crystallization time of 60 s. Subsequently, the THT stock solution added to 10 ml EtOH was dropped onto a quartz substrate with crystallized TDP cocrystals. The volume ratio of the TDP to THT mixture was 1:10 to 1:20. When the solvents evaporated completely, organic semi-wrapped heterostructures were observed from the substrate.

Hierarchical self-assembly of the organic vertically superposed heterostructures

0.02 mmol (3.6 mg) of TCNB and 0.02 mmol (7.2 mg) of HDP were dissolved in 10 mL DCM at a concentration of 2.0 mmol L⁻¹ to obtain the TDP stock solution. Similarly, a THT stock solution was prepared by dissolving 0.02 mmol (3.6 mg) of TCNB and 0.02 mmol (4.6 mg) of BHT into 10 ml of DCM at a concentration of 2.0 mmol L⁻¹. Then, the TDP stock solution was added to 10 ml of EtOH, and 100 μ L of the mixed solution was dropped onto a quartz substrate with a crystallization time of 60 s. Subsequently, the THT stock solution was added to 10 ml of EtOH, and 1500 μ L of the mixed solution was dropped onto a quartz substrate with a crystallized TDP cocrystal. When the crystallization time reached 60 s, 350 μ L of the TDP mixed solution was dropped onto the substrate again, and when the solvent evaporated completely, vertically superposed organic heterostructures were observed from the substrate.

Data availability

All data generated in this study are provided in the paper or Supplementary Information. Additional data related to this paper may be requested from the authors. Crystallographic data are available free of charge from the Cambridge Crystallographic Data Center (CCDC 2334148; 2085053).

References

- Kim, J. Y. et al. Efficient tandem polymer solar cells fabricated by all-solution processing. *Science* **317**, 222–225 (2007).
- Lv, Q. et al. Lateral epitaxial growth of two-dimensional organic heterostructures. *Nat. Chem.* **16**, 201–209 (2024).
- Geim, A. K. & Grigorieva, I. V. Van der Waals heterostructures. *Nature* **499**, 419–425 (2013).
- Sun, C. et al. Single-chip microprocessor that communicates directly using light. *Nature* **528**, 534–538 (2015).
- Zhang, C. et al. One-dimensional organic photonic heterostructures: rational construction and spatial engineering of excitonic emission. *Adv. Mater.* **24**, 1703–1708 (2012).
- Yao, Y. et al. Heteroepitaxial growth of multiblock Ln-MOF microrods for photonic barcodes. *Angew. Chem. Int. Ed.* **131**, 13941–13945 (2019).
- He, F., Gadt, T., Manners, I. & Winnik, M. A. Fluorescent “barcode” multiblock co-micelles via the living self-assembly of di- and triblock copolymers with a crystalline core-forming metalblock. *J. Am. Chem. Soc.* **133**, 9095–9103 (2011).
- Zhuo, M. P. et al. Visualizing the interfacial-layer-based epitaxial growth process toward organic core-shell architectures. *Nat. Commun.* **15**, 1130 (2024).
- Yamamoto, Y. H. et al. Photoconductive coaxial nanotubes of molecularly connected electron donor and acceptor layers. *Science* **314**, 1761–1764 (2006).
- Zhao, J. Y. et al. Full-color laser displays based on organic printed microlaser arrays. *Nat. Commun.* **10**, 870 (2019).
- Kong, Q. et al. Epitaxial self-assembly of binary molecular components into branched nanowire heterostructures for photonic applications. *J. Am. Chem. Soc.* **136**, 2382–2388 (2014).
- Zheng, J. Y. et al. Wire-on-wire growth of fluorescent organic heterojunctions. *J. Am. Chem. Soc.* **134**, 2880–2883 (2012).
- Lv, Y. et al. All-color subwavelength output of organic flexible microlasers. *J. Am. Chem. Soc.* **139**, 11329–11332 (2017).
- Nguyen, A. T. et al. Crystal networks in silk fibrous materials: from hierarchical structure to ultra performance. *Small* **11**, 1039–1054 (2015).
- Wang, K. et al. Stimulated emission-controlled photonic transistor on a single organic triblock nanowire. *J. Am. Chem. Soc.* **140**, 13147–13150 (2018).
- Zhang, Y. et al. Organic single-crystalline p–n junction nanoribbons. *J. Am. Chem. Soc.* **132**, 11580–11584 (2010).
- Pradeep, V. V. et al. Mechanical processing of naturally bent organic crystalline microoptical waveguides and junctions. *Small* **17**, 2006795 (2021).
- Zhuo, M. P., He, G. P., Wang, X. D. & Liao, L. S. Organic superstructure microwires with hierarchical spatial organization. *Nat. Commun.* **12**, 2252 (2021).
- Bolla, G. et al. Cocrystallization tailoring multiple radiative decay pathways for amplified spontaneous emission. *Angew. Chem. Int. Ed.* **60**, 281–289 (2021).
- Lan, L., Liu, H., Yu, X., Liu, X. & Zhang, H. Polymer-coated organic crystals with solvent-resistant capacity and optical waveguiding function. *Angew. Chem. Int. Ed.* **60**, 11283–11287 (2021).
- Ye, X. et al. 1D versus 2D cocrystals growth via microspacing in-air sublimation. *Nat. Commun.* **10**, 761 (2019).
- Lee, J. W. et al. Light-emitting rubrene nanowire arrays: a comparison with rubrene single crystals. *Adv. Funct. Mater.* **19**, 704–710 (2009).
- Sirringhaus, H. et al. High-resolution inkjet printing of all-polymer transistor circuits. *Science* **290**, 2123–2126 (2000).
- Venkataramudu, U., Venkatakrishnarao, D., Chandrasekhar, N., Mohiddon, M. A. & Chandrasekar, R. Single-particle to single-particle transformation of an active type organic μ -tubular homostucture photonic resonator into a passive type hetero-structure resonator. *Phys. Chem. Chem. Phys.* **18**, 15528–15533 (2016).
- Venkatakrishnarao, D., Mohiddon, M. A., Chandrasekhar, N. & Chandrasekar, R. Photonic microrods composed of photoswitchable molecules: erasable heterostructure waveguides for tunable optical modulation. *Adv. Opt. Mater.* **3**, 1035–1040 (2015).
- Flöry, N. et al. Waveguide-integrated van der Waals heterostructure photodetector at telecom wavelengths with high speed and high responsivity. *Nat. Nanotechnol.* **15**, 118–124 (2020).
- Zhang, W. et al. Supramolecular linear heterojunction composed of graphite-like semiconducting nanotubular segments. *Science* **334**, 340–343 (2011).
- Ma, Y. et al. Oriented self-assembly of hierarchical branch organic crystals for asymmetric photonics. *J. Am. Chem. Soc.* **145**, 9285–9291 (2023).

29. Lu, T. & Chen, F. W. Multiwfn: a multifunctional wavefunction analyzer. *J. Comput. Chem.* **33**, 580–592 (2012).
30. Dadfarnia, M. et al. Recent advances in the study of structural materials compatibility with hydrogen. *Adv. Mater.* **22**, 1128–1135 (2010).
31. Adams, I. & Bancroft, G. M. Solution evaporation method for solid state ESCA studies. *Nature* **250**, 219–220 (1974).
32. Jang, J. et al. Highly crystalline soluble acene crystal arrays for organic transistors: mechanism of crystal growth during dip-coating. *Adv. Funct. Mater.* **25**, 1005–1014 (2012).
33. Ganda, S. & Stenzel, M. H. Concepts, fabrication methods and applications of living crystallization-driven self-assembly of block copolymers. *Prog. Polym. Sci.* **101**, 101195 (2020).
34. Wang, X., Li, H., Wu, Y., Xu, Z. & Fu, H. Tunable morphology of the self-assembled organic microcrystals for the efficient laser optical resonator by molecular modulation. *J. Am. Chem. Soc.* **136**, 16602–16608 (2014).
35. Gavezzotti, A. & Filippini, G. Polymorphic forms of organic crystals at room conditions: thermodynamic and structural implications. *J. Am. Chem. Soc.* **117**, 12299–13305 (1995).
36. Sun, L. J. et al. Thermally activated delayed fluorescence in an organic cocrystal: narrowing the singlet–triplet energy gap via charge transfer. *Angew. Chem. Int. Ed.* **131**, 11433–11438 (2019).
37. Hu, X., Jiang, P., Ding, C., Yang, H. & Gong, Q. Picosecond and low-power all-optical switching based on an organic photonic-bandgap microcavity. *Nat. Photonics* **2**, 185–189 (2008).
38. Clark, J. & Lanzani, G. Organic photonics for communications. *Nat. Photonics* **4**, 438–446 (2010).
39. Ravi, J. et al. Geometrically reconfigurable, 2D, all-organic photonic integrated circuits made from two mechanically and optically dissimilar crystals. *Adv. Funct. Mater.* **31**, 2105415 (2021).
40. Ravi, J. & Chandrasekar, R. Micromechanical fabrication of resonator waveguides integrated four-port photonic circuit from flexible organic single crystals. *Adv. Opt. Mater.* **9**, 2100550 (2021).
41. Bragheri, F., Faccio, D., Romagnoli, M., Krauss, T. & Roberts, J. Effects of random and systematic perturbations in a one-dimensional photonic crystal wavelength converter. *Phys. Rev. E* **70**, 017601 (2004).
42. Lanzaò, L. et al. Encoding and decoding spatio-temporal information for super-resolution microscopy. *Nat. Commun.* **6**, 6701 (2015).
43. Zhang, C., Zheng, J. Y., Zhao, Y. S. & Yao, J. Self-modulated white light outcoupling in doped organic nanowire waveguides via the fluctuations of singlet and triplet excitons during propagation. *Adv. Mater.* **23**, 1380–138 (2011).
44. Sun, M. J. et al. In situ visualization of assembly and photonic signal processing in a triplet light-harvesting nanosystem. *J. Am. Chem. Soc.* **140**, 4269–4278 (2018).
45. Lattante, S., Creti, A., Lomascolo, M. & Anni, M. On the correlation between morphology and amplified spontaneous emission properties of a polymer: polymer blend. *Org. Electron.* **29**, 44–49 (2016).
46. Zhuo, M. P. et al. Hierarchical self-assembly of organic core/multi-shell microwires for trichromatic white-light sources. *Adv. Mater.* **33**, 2102719 (2021).
47. Wu, B. et al. Organic bilayer heterostructures with built-in exciton conversion for 2D photonic encryption. *Adv. Mater.* **35**, 2306541 (2023).
48. Chandrasekhar, N., Mohiddon, M. A. & Chandrasekar, R. Organic submicro tubular optical waveguides: self-assembly, diverse geometries, efficiency, and remote sensing properties. *Adv. Opt. Mater.* **1**, 305–311 (2013).

Acknowledgements

The authors acknowledge the financial support from the National Natural Science Foundation of China (no. 52173177, X.-D. W.), the Natural Science Foundation of Jiangsu Province (no. BK20221362, X.-D. W.), and the Natural Science Foundation of Jiangsu Province (no. BK20230010, X.-D. W.). Furthermore, this project is funded by the Jiangsu Key Laboratory for Carbon-Based Functional Materials & Devices, Soochow University (KJS2156, X.-D. W.), Collaborative Innovation Center of Suzhou Nano Science & Technology, the 111 Project, Joint International Research Laboratory of Carbon-Based Functional Materials and Devices, and Soochow University Tang Scholar.

Author contributions

X.-D.W. designed the experiments. Y.-X.M. synthesized the organic crystals and performed the structural and optical characterization. Y.-X.M. and X.-D.W. discussed the results and wrote the paper. All authors discussed the results and commented on the manuscript.

Competing interests

The authors declare no competing interests.

Additional information

Supplementary information The online version contains supplementary material available at <https://doi.org/10.1038/s41467-024-52187-8>.

Correspondence and requests for materials should be addressed to Xue-Dong Wang.

Peer review information *Nature Communications* thanks Mei-Jin Lin and the other, anonymous, reviewer for their contribution to the peer review of this work. A peer review file is available.

Reprints and permissions information is available at <http://www.nature.com/reprints>

Publisher's note Springer Nature remains neutral with regard to jurisdictional claims in published maps and institutional affiliations.

Open Access This article is licensed under a Creative Commons Attribution-NonCommercial-NoDerivatives 4.0 International License, which permits any non-commercial use, sharing, distribution and reproduction in any medium or format, as long as you give appropriate credit to the original author(s) and the source, provide a link to the Creative Commons licence, and indicate if you modified the licensed material. You do not have permission under this licence to share adapted material derived from this article or parts of it. The images or other third party material in this article are included in the article's Creative Commons licence, unless indicated otherwise in a credit line to the material. If material is not included in the article's Creative Commons licence and your intended use is not permitted by statutory regulation or exceeds the permitted use, you will need to obtain permission directly from the copyright holder. To view a copy of this licence, visit <http://creativecommons.org/licenses/by-nc-nd/4.0/>.

© The Author(s) 2024